Efficient Spectroscopic Imaging by an Optimized Encoding of Pretargeted Resonances

Zhiyong Zhang,[1,2] Noam Shemesh,[1,3] and Lucio Frydman[1]*

Purpose: A "relaxation-enhanced" (RE) approach to acquire in vivo localized spectra with flat baselines and good sensitivity has been recently proposed. As RE MR spectroscopy (MRS) targets a subset of a priori known resonances, new possibilities arise to acquire spectroscopic imaging data in faster, more efficient manners. This is hereby illustrated by Spectroscopically Encoded Chemical Shift Imaging (SECSI).

Methods: SECSI delivers spectral/spatial correlations by collecting gradient echo trains whose timings are defined by the shifts of the resonances to be disentangled. Condition number considerations allow one to unravel these image contributions for various sites by a simple matrix inversion. The efficiency of the ensuing method is high enough to enable a sampling of additional spatial axes by means of their phase encoding in spin-echo trains.

Results: The one-dimensional (1D) spectral / 2D spatial SECSI acquisitions were implemented on phantom, ex vivo, and in vivo models. In all cases, quality site-resolved images were obtained. The experimentally observed enhancements were consistent with theoretical signal-to-noise ratio derivations.

Conclusion: While still bound by MRSI's sensitivity limitations, a novel spectroscopic imaging protocol exploiting a priori information, selective excitations and multiple echo encodings, was proposed and demonstrated. The method is promising when dealing with high T_2/T_2^* ratios, sparse data, or hyperpolarization studies. **Magn Reson Med 77:511–519, 2017.** © **2016 International Society for Magnetic Resonance in Medicine**

Key words: MRSI; brain metabolic imaging; selective spectral excitations

INTRODUCTION

MRI and MR spectroscopy (MRS) play crucial roles in deciphering the relationship between structure, function and metabolism (1,2). Combining MRS and MRI into a single MR spectroscopic imaging (MRSI) data set (3) is challenged by the need to (i) resolve chemical shifts along a spectral dimension requiring fairly long (~100 ms) acquisition times; (ii) impart the spatial encoding using indirectly detected phase-encoded dimensions; (iii) limit the repetition rate of these experiments according to the long T_1 values that may characterize the metabolites; and (iv) actively suppress the ca. $10^4 \times$ more intense water resonance falling in the center of the 0–10 ppm ^{1}H chemical shift range usually targeted. In particular, this overwhelming water peak perturbing the metabolic resonances and the spectral baseline, generally demands the use of efficient water suppression sequences (4–7). Alternative approaches avoid this and excite water together with the targeted metabolites, relying on a large dynamic receiving range to avoid saturation (8–10). Recent studies have demonstrated the convenience of carrying out ^{1}H MRS using highly selective pulses, targeting only the frequencies of a priori known resonances of interest (11,12). Driving the use of these selective excitations is the fact that, although numerous chemicals can in principle be resolved in brain (3), most studies focus on few, prominent resonances associated to specific metabolites. It has been shown that at ultrahigh fields in particular, so-called "relaxation-enhanced" (RE) methods that carefully craft selective excitation pulses targeting the prominent resonances of creatine (Cre), choline (Cho), N-Acetyl-Asparate (NAA), and lactic acid (Lac), enable the acquisition of in vivo localized spectra with flat baselines and excellent signal-to-noise ratios (SNRs) in a single scan (11–14). A sensitivity enhancement was noticed for these experiments vis-à-vis lower field counterparts using conventional water-suppressed MRS, reflecting an enhanced longitudinal relaxation arising from a proton bulk reservoir that is left mostly unperturbed, and from relaxation properties that at ultrahigh fields benefit the metabolic resonances over the water counterparts.

With this as background, the question arises on the optimal way of endowing RE MRS experiments with imaging capabilities. The fact that RE MRS transforms an in-principle continuous spectral acquisition into a sparse one targeting a small number of resonances whose positions are a priori known, opens new possibilities to acquire MRSI information in a faster, more efficient manner. Indeed, with frequencies known, the images of the various targeted metabolites can in principle be resolved by collecting a series of conventional imaging data sets, where the chemical shifts of the different resonances have been differentially encoded by specific phase modulations. Such chemical shift encoding has been demonstrated in the past, using either phase-modulated pulses

[1]Department of Chemical Physics, Weizmann Institute of Science, Rehovot 76100, Israel.

[2]Department of Electronic Science, Xiamen University, Xiamen, Fujian 361005, China.

[3]Champalimaud Neuroscience Programme, Champalimaud Centre for the Unknown, Lisbon, Portugal.

Grant sponsor: the Israel Science Foundation; Grant number: 795/13; Grant sponsor: the Kimmel Magnetic Resonance Institute (Weizmann), by ERC-2014-PoC; Grant number: 633888; Grant sponsor: the Perlman Family Foundation; Grant sponsor: the China Scholarship Council; Grant number: 201306310056.

*Correspondence to: Prof. Lucio Frydman, Department of Chemical Physics, Weizmann Institute of Science, Rehovot 76100, Israel.
E-mail: lucio.frydman@weizmann.ac.il

Received 9 November 2015; revised 11 January 2016; accepted 20 January 2016

DOI 10.1002/mrm.26161

Published online 23 February 2016 in Wiley Online Library (wileyonlinelibrary.com).

© 2016 International Society for Magnetic Resonance in Medicine

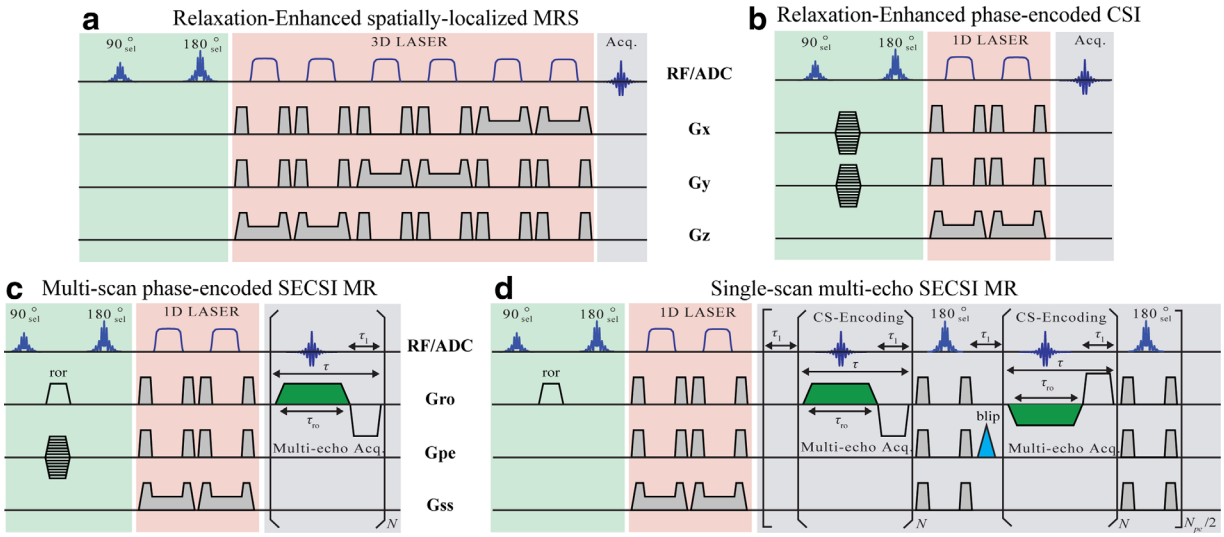

FIG. 1. Principles of SECSI MRSI. **a**: Basic RE MRS sequence (11,13) incorporating a 90° SLR multiband selective pulse, a series of 180° pulses providing refocusing and 3D LASER localization, and a FID acquisition. **b**: Chemical shift imaging (CSI) extension, endowed with 2D spatial resolution by the addition of two phase-encoding gradients. **c**: SECSI MR sequence extracting the spectroscopic information by means of *N* refocused readout gradients whose echoes are timed at intervals τ that enable, following an FT of the echoes along their k_{ro}-evolution axes, a stable matrix-based inversion delivering each of the metabolites' images. A τ_1 delay is introduced to refocus the gradient-imposed evolution without disturbing these shift-encoding steps. **d**: Single-shot SECSI extension of (c), incorporating a CPMG-based echo train that phase-encodes one spatial dimensions in a single N_{pe}-loops scan. In (b), (c) and (d), the spatial encoding of the MRS information is assumed along only two axes, leaving a need for a 1D LASER block to localize the remaining dimension.

or suitable delay times imparted in different scans (15–17). The present study describes the principles, implementation, and potential advantages of alternative MRSI forms based on imparting the modulations in unison with gradient echo trains, in what we denote as Spectroscopically Encoded Chemical Shift Imaging (SECSI) MR.

METHODS

Principles of SECSI

The starting point of this study is the RE MRS sequence shown in Figure 1a (11). This incorporates a 90° pulse exciting solely *M* bands containing the metabolites of interest, while minimizing the water resonance's excitation. As achieving such selectivity requires a relatively long pulse the experiment is executed in a spin-echo format, incorporating a refocusing pulse (18,19) that solely addresses the excited bands. To complement the spectral selectivity of these pulses with spatial selectivity, RE MRS incorporates three adiabatic LASER pulse pairs (20) that circumscribe the observed region to a rectangular voxel in space.

On considering how to extend this localized MRS scheme to MRSI, the simplest option is to complement the LASER localization with phase-encoding of the spatial dimensions. Figure 1b illustrates the resulting chemical shift imaging (CSI) sequence (21,22), assuming the encoding of two spatial axes and a LASER-based slice selection along the third one. While enjoying the potential benefits from relaxation enhancement, this scheme suffers from a long intrinsic acquisition time. This can be shortened by noticing a redundancy in this experiment, which assumes a priori known peak positions for performing the excitation, but at the same time devotes a full time-domain acquisition to characterize the same frequency peaks.

To solve this redundancy we introduce a "signature" in the form of peak-dependent phase modulations, whose aim will be to provide the image corresponding to each resonance without demanding a full Fourier analysis of the free induction decay (FID). This can be implemented either by the addition of suitable phase factors upon performing the spectral excitation (23,24), or by introducing an array of suitably timed delays. Figure 1c illustrates the latter implementation, which builds on the RE CSI sequence in Figure 1b, but replaces one of the phase-encoded loops by a combination of shift-encoding time delays and spatial-encoding gradient echoes. RE MRS's excitation and refocusing of the $\{\Omega_m\}_{1\leq m\leq M}$ targeted resonances/bands thus remain unchanged, and so does the slice selection carried out by the one-dimensional (1D) LASER block. The acquisition, however, is now replaced by a train of *N* readout gradients ($N \geq M$), incorporating gradient echoes at a set of suitable intervals $\{\tau_n\}_{1\leq n\leq N}$. Each of these gradient echoes will be part of a full imaging set, where the contribution of each site will be modulated by individual chemical shift factors $e^{i(\Omega_m \tau_n)}$. Assuming that each image acquisition segment is sufficiently short to disregard intrasegment modulations (i.e., $|\Omega_k\text{-}\Omega_j|.\tau_n << 1\ \forall k, j$), and given that each image acquisition is followed by a full gradient echo, it is possible to describe the *n-th* observed echo signal as:

$$s_n(k,\Omega_m)=\sum_{m=1}^{M}\int \rho(r,\Omega_m)\cdot e^{ikr}e^{i(\Omega_m\tau_n)}dr,\quad n=1,2,\ldots,N \qquad [1]$$

Fourier transformation (FT) of each of these k-space signals yields a set of N images

$$I_n(r,\Omega_m)=\sum_{m=1}^{M}\rho(r,\Omega_m)\cdot e^{i(\Omega_m\tau_n)},\quad n=1,2,\ldots,N \qquad [2]$$

Notice that each of these images mixes contributions from all the spectral counterparts, with their phases modulated by an encoding $E_{mn}=\{e^{i(\Omega_m\tau_n)}\}$ matrix. Rather than choosing this encoding matrix according to Nyquist criteria, we choose the time intervals $\{\tau_n\}_{1\le n\le N}$ so as to endow E_{mn} with a low condition number. This opens the possibility of stably inverting Eq. [2], and thereby of separating algebraically the various $\rho(r,\Omega_m)$ contributions. Many routes could be devised for finding such optimum set of time intervals for a given subset of resonances of interest. In the present study, a simple approach was adopted, whereby all encoding delays were set multiples of a basic interval τ: $\tau_n=n\tau$, $n=1, 2, \ldots, N$. Searching for a stable inversion of the chemical shift encoding matrix E becomes then a straightforward search for the matrix's minimum condition number, for instance, using Matlab's® (The MathWorks, Natick, MA) "*cond*(*E*)" script, as a function of two parameters: τ and N. Inversion of this well-conditioned E yields a stable decoding transformation matrix D_{mn}, delivering "pure" images for individually separated resonance as:

$$\rho(r,\Omega_m)=\sum_{n=1}^{N}D_{m,n}\cdot I_n(r,\Omega_m). \qquad [3]$$

A further improvement associated with this encoding mode, relates to the fact that the overall time $T_{acq}=N\tau$ required to encode a small number of resonances will be typically short; much shorter than the acquisition boundaries placed by typical metabolic T_2s. This opens the possibility of extending the 1D phase-encoded gradient-echo scheme in Figure 1c to a single-shot sequence involving both gradient- and spin-echoes (25,26), as shown in Figure 1d. In this sequence, a Carr-Purcell Meiboom-Gill (CPMG) scheme probes in a single shot what was a phase-encoded dimension (27,28), incorporating this encoding as a series of N_{pe} blips. The addition of 180° refocusing pulses, kept selective and circumscribed to an even number to ensure that the bulk reservoir of unexcited magnetization remains unperturbed, brings about periodic reversals in the chemical shift evolution; this amounts to switching between $\{E_{mn}\}$ and $\{E^*_{mn}\}$ chemical shift encoding matrices for each phase encoding step. To maintain a steady sampling of the signal near the k-origin, these refocusing pulses necessitate as well a reversal in the signs of the readout gradients between even and odd spin-echoes. Moreover, when considering the arrangement of the chemical shift encoding elements in the generalized (k_{ro},k_{pe},τ_n) 3D space where the spin evolution associated to this experiment takes place, the shift-related evolution advances in a "positive" way in the first N readout echoes, and reverses its progress in the next subsequent N echoes. In other words a modulation $\{E_{mn}\}$ drives the chemical shift encoding before the odd 180° pulses, whereas its complex conjugate $\{E^*_{mn}\}$ defines the shift encoding before the even ones. Assuming that the readout and phase encodings are associated to x and y axes, respectively, one can extend the shift-encoding expression in Eq. [1] to:

$$s_n(k_x,k_y,\Omega_m)=\sum_{m=1}^{M}\left[\int_Y\int_X \rho(x,y,\Omega_m)\cdot e^{ik_xx}e^{ik_yy}e^{i(\Omega_m n\tau)}dxdy\right]. \qquad [4]$$

Arguments akin to those leading to Eq. [3] but relying on a 2D FT with respect to k_x, k_y, lead to a series of "pure" images for each of the addressed resonances, $\{\rho(x,y,\Omega_m)\}_{m=1,2,\ldots,M}$. A full description of this sampling scheme and the overall experimental setup, is summarized in the Supporting Information 1, which is available online.

Signal-to-Noise Considerations

It is worth assessing the relative sensitivity merits of the MRSI variants introduced in the previous paragraph; more specifically, of the alternatives summarized in Figures 1b, 1c and 1d. As all these schemes rely on the same excitation and refocusing pulses, share the same LASER volume localization and are endowed with similar echo times, one can assume that their overall efficiencies are equal. Furthermore, we shall assume that, in their image spaces, equal fields of view (FOVs) are targeted and endowed by equal matrix sizes N_x, N_y. It follows (29) that the SNR of all these imaging methods can then be summarized as

$$SNR\propto\frac{A}{\sqrt{\Delta f}}\cdot\frac{f_x}{\sqrt{N_x}}\cdot\frac{f_y}{\sqrt{N_y}}\cdot\frac{f_\delta}{\sqrt{N_\delta}}, \qquad [5]$$

where A is the initial time-domain amplitude of all the FIDs, Δf represents the receiver bandwidth that needs to be chosen to suit these experiments' needs; f_x, f_y and f_δ are terms describing the SNR enhancement associated to transforming the signals from their acquired domains into the two spatial and single spectral domains, respectively; and N_δ is associated to the number of elements that will be present in the spectral dimension. The meaning of the f-functions becomes clear if considering, for example, the spatial dimensions of the RE CSI experiment (Fig. 1b): in such instances they will reflect the multiplexing brought about by the FT along the k-axes, leading to $f_x=N_x$, $f_y=N_y$. Fourier transform along the spectral domain δ will in turn lead to a signal enhancement $f_\delta=\frac{N_\delta}{t^\delta_{acq}}\int_0^{t^\delta_{acq}}e^{-t/T_2^*}dt$, where t^δ_{acq} is the overall FID sampling time, N_δ the number of sampled points, T_2^* the inhomogeneous spin–spin decay time, and the integral accounts for the fact that the experiment involves a spin echo. As the bandwidth in such spectral acquisition is set as $\Delta f=N_\delta/t^\delta_{acq}$, replacement of all these factors into Eq. [5] leads to

$$SNR_{CSI} = \frac{A\sqrt{N_x}\cdot\sqrt{N_y}}{\sqrt{t^{\delta}_{acq}}}\int_0^{t^{\delta}_{acq}} e^{-t/T_2^*}\,dt \qquad [6]$$

A similar analysis can be applied to the multiscan SECSI sequence in Figure 1c, if accounting for the facts that (i) spectral information is now obtained by a matrix-based decoding process, and (ii) the actual data sampling is performed while under the action of a readout gradient. Given the low condition number of the spectral decoding matrix, its efficiency can be considered nearly equal to that of an FT. Thus, in analogy what was done in the CSI case for the spatial axes, the spectral multiplexing advantage can be described as $\frac{f_\delta}{\sqrt{N_\delta}} = \sqrt{N}$, where N is the number of spectral encoding loops as introduced in Eq. [1]. Taking into account that the encoding along the phase-encoded axis stayed unchanged and that the readout axis now imposes $\Delta f = N_x/\tau_{ro}$, where $\tau_{ro} = \tau - \tau_1$ is the time associated to the data sampling of a gradient echo, the analogue of Eq. [6] for a multiscan SECSI acquisition becomes

$$SNR^{multi-scan}_{SECSI} \propto \frac{A\cdot\sqrt{N}\cdot\sqrt{N_{pe}}}{\sqrt{\tau_{ro}}}\cdot\int_{-\tau_{ro}/2}^{\tau_{ro}/2} e^{-|t|/T_2^*}\,dt \qquad [7]$$

Finally, this analysis can be extended to the single-scan SECSI sequence in Figure 1d, by replacing the FT leading in Eqs. [6] and [7] to the $\sqrt{N_y}$ and $\sqrt{N_{pe}}$ enhancing factors, with a proper summation over the N_{pe} phase-encoding echoes involved in the acquisition:

$$SNR^{multi-scan}_{SECSI} \propto \frac{A\cdot\sqrt{N}\cdot\sqrt{N_{pe}}}{\sqrt{\tau_{ro}}}\cdot\int_{-\tau_{ro}/2}^{\tau_{ro}/2} e^{-|t|/T_2^*}\,dt \cdot\frac{\sum_{j=1}^{N_{pe}}\exp[-j(N\tau+\Delta)/T_2]}{\sqrt{N_{pe}}} \qquad [8]$$

here Δ is the delay associated with the gradient blips and CPMG refocusing pulses, and T_2 is a homogeneous spin–spin relaxation time characterizing the decay of the CPMG train.

Before concluding it is worth remarking that although Eqs. [6]–[8] summarize the idealized SNR for all these acquisitions modes assuming similar excitation efficiencies, repetition times and imaging characteristics, the number of scans that are involved in reaching these 3D spectral/spatial data sets are very different: they involve at least $N_x \times N_y$ shots for RE CSI, N_{pe} $(= N_y)$ shots for multiscan SECSI, and a single shot for the single-scan SECSI. Hence the efficiency per unit acquisition time made by these experiments will differ, and will in fact be given by the number N of targeted peaks and by the T_2, T_2^* characteristics. We compare below how experimental observations follow these theoretical predictions.

Experimental

The performance of these approaches was assayed on two phantoms composed of four components: one made up of water, NAA, Cho, and Cre; the other involving water, methanol, acetone, cyclohexane. Experiments also focused on a fresh ex vivo rat brain sample targeting NAA, total cholines (tCho), and total creatine (tCre) resonances, and on a mouse's abdomen for the sake of exploring water/fat separation. These acquisitions were carried out on a 7 Tesla (T)/120 mm horizontal magnet MRI using a quadrature birdcage coil probe, and on a 14.1T/89 mm vertical bore magnet using a linear Millipede® probe, both of these Varian Inc. (Palo Alto, CA) systems.

As an aid in setting up the sequences in Figure 1, spin-echo multislice (SEMS) imaging, point-resolved (PRESS) and LASER-based localized spectroscopy experiments were also carried out, using sequences taken from the scanner's software libraries. To better assess the performance of the multi- and single-shot SECSI sequences, these were also compared against the more conventional multiscan CSI approach shown in Figure 1b. Spectroscopically resolved images in these 2D phase-encoded experiments were obtained by targeting the individual spectral resonances, whose images were integrated over their respective peak widths. Radiofrequency (RF) pulses in all these sequences were designed on the basis of the SLR algorithm (30), computed using a Matlab® script, and uploaded onto the scanner for execution.

Optimization of the number and duration of the encoding delays based on the conditioning of the chemical shift encoding matrix $\{E_{mn}\}$ (possessing an identical inversion stability as $\{E^*_{mn}\}$), were also carried out using Matlab scripts. All the data rearrangements, phase corrections, and shift decoding procedures were written as embedded macros in the scanner's original VNMRJ® programming environments; this provided the possibility of executing the image/spectral processing directly within the acquisition environment, and benefiting from the Fourier processing, phase correction, and image display capabilities inherent to the scanner's interface. All of these Matlab and VNMRJ preparation and processing scripts and macros are available upon request.

Animal protocols and maintenance were done in accordance with guidelines of the Institutional Committee on Animals of the Weizmann Institute of Science (IACUC protocol 10790514). For the ex vivo experiments, rat brain specimens were extracted by surgery and immersed into a phosphate buffer solution (PBS, 0.1 M, pH 7.4) immediately after their extraction; following a brief wash, these were inserted into a 15-mm glass tube filled with Fluorinert® under bubble-free conditions. Gauze was used to fix the position and preserve the structural integrity of these brains, which were allowed to equilibrate inside the magnet for approximately 30 min before performing their MR data acquisition at 22°C. The fluorinated solvent prevented the loss of metabolites throughout the MRSI experiments, as ascertained by comparing 1D MRS data before and after the CSI and SECSI runs (Supporting Information, Fig. S2). No specimen was scanned for over 12 h. In vivo experiments were performed while mice were anesthetized with Isoflurane (Abbott Laboratories Ltd, England; 3% for induction, 1–2% for maintenance) mixed with oxygen (1 L/min) delivered through a nasal mask. Respiration throughout the exam was monitored using an SA Instruments Model 1025 monitoring and gating system

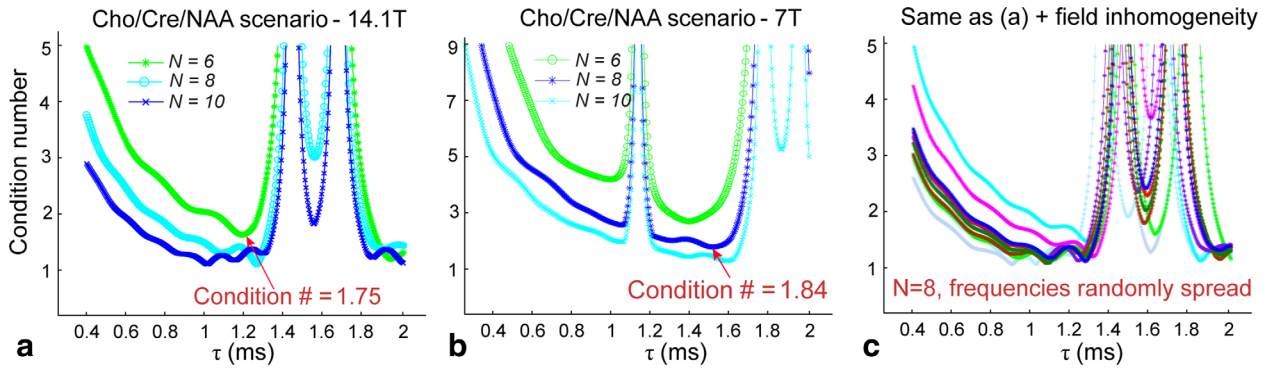

FIG. 2. Optimizing the condition number of a chemical shift encoding matrix $E_{mn} = \{e^{i(\Omega_m n\tau)}\}$, assuming $\tau_n = n\tau$, $n = 1,\ldots, N$. **a**: 14.1T phantom sample scenario involving Cho, Cre and NAA methyl peaks at 3.09, 2.93, and 1.92 ppm, showing how condition numbers change as a function of τ and N. **b**: Idem but for a 7T scenario. **c**: Examining the robustness of E's conditioning, with ten cases where the frequencies of the three resonances targeted in (a) were varied randomly over 40 Hz, for N fixed at eight gradient echoes.

(Stony Brook, NY), and maintained throughout the experimental period at 50–70 breaths per min by adjusting the isoflurane levels. Body temperature was maintained at approximately 37°C using a thermostatized fluid system.

RESULTS

Figure 2 exemplifies how the $\{\tau_n = n\cdot\tau\}_{1\le n\le N}$ arrays defining the chemical shift encoding matrices required for SECSI were chosen, for different sets of predefined chemical shifts. The left-hand panel of Figure 2 shows the changes in the encoding's matrix $\{E_{mn}\}$ condition number as a function of the two parameters (N and τ) involved. These calculations assumed a 14.1T excitation addressing the methyl peaks of Cho, Cre, and NAA, resonating at 3.09, 2.93, and 1.92 ppm, respectively. As follows from these graphs a suitable number of gradient echoes per phase encoding step arises when $N = 6$ and $\tau = 1.18$ ms (Fig. 2a); the ensuing condition number (1.75) is sufficiently low to ensure a stable matrix inversion, while the encoding duration is sufficiently short to enable the implementation of CPMG acquisitions. Slightly shorter and longer values provide even better condition numbers for $N = 10$ and 8, respectively, yet at the expense of increasing the overall $N\tau$ encoding time.

The center panel of Figure 2 shows an extension of this test to 7T. Under these conditions $N = 8$ gradient echoes lead to a good condition number at $\tau = 1.52$ ms (Fig. 2b); again, although an $N = 10$ train would lead to a lower condition number, the overall encoding time ($\approx 10 \times 1.62$ ms) would be too long to justify the ensuing gain. Another aspect analyzed in Figure 2c, is how disturbances in the presumed chemical shifts will affect the method's site separation abilities. It can be readily shown that, if the changes originate from relatively small field heterogeneities, so that at a single-voxel level all the peaks to be resolved move in unison, the condition number of the encoding matrix will remain unchanged. Likewise, coherent field fluctuations of the kind usually associated with motions, should not affect the efficiency of the spectral decoding. If field heterogeneities become so large that even within a given voxel the peaks exhibit a relative fluctuation with respect to one another, $\{E_{mn}\}$'s condition number changes. As evidenced by Figure 2c, these random changes will have only minor effects in the inversion properties of the encoding matrix, evidencing the method's robustness vis-à-vis larger field heterogeneities. Overall, these examples demonstrate that low condition numbers can usually be found for sparse spectral scenarios like the ones addressed by RE MRS; phantom-based experiments presented in Supporting Information Figure S3, illustrate this robustness of the method against inhomogeneities.

Figure 3 compares the relative SNRs and residual cross-talk levels among the different locations of various chemical sites of SECSI and of optimized relaxation-enhanced CSI experiments. These tests examined a phantom consisting of an outer water tube, and three inner tubes with Cho, Cre, and NAA (labeled as I, II, III, respectively; Figure 3a). The spectra in Figures 3b and 3c illustrate the good water suppression and quality data achieved by the selective excitation protocol. Figures 3d–f demonstrate that all sequences successfully separate the three targeted chemical shifts, and provide quality 2D images for each. Similar levels of cross-talk artifacts are evidenced by the 2D phase-encoded CSI results (Fig. 3d) as for their SECSI-based counterparts (Figs. 3e,f). To better assess the relative SNR performance of the different approaches all experiments were collected with equal FOVs and in-plane resolutions (parameters that were also assumed equal in the SNR derivations presented earlier).

Experiments in Figures 3d–f were also collected with a relatively long TR = 5 s to factor out potential saturation considerations. Still, given the very different minimum durations of the various experiments, the number of scans collected was tailored according to each sequence; this signal averaging difference was accounted for in SNR calculations by renormalizations as per $\sqrt{}$#scans. With these provisions, we compare the results summarized in the various panels of Figure 3 with the theoretical expectations arising from Eqs. [6]–[8]. The multiscan SECSI *vs* the CSI data for peaks I–III (Figs. 3d,e) show an average sensitivity ratio between the two of 0.56; when factoring the fact that the former involved eight averaged scans while the latter only one, the experimental per-scan ratio becomes $SNR_{SECSI}^{multi-scan}/SNR_{CSI} \approx 0.199$. The

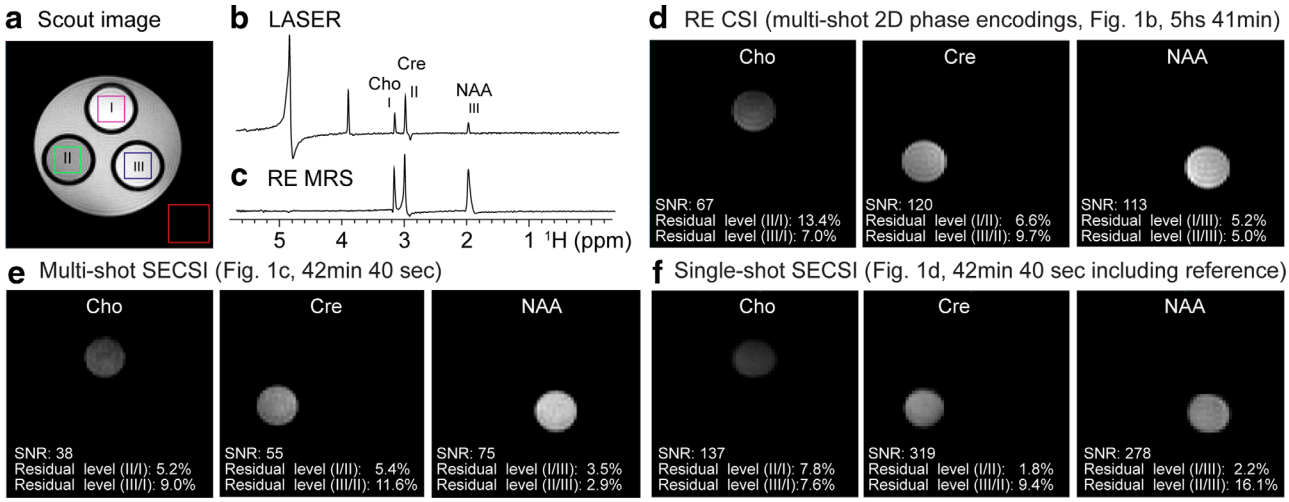

FIG. 3. The 14.1T spectroscopic imaging results collected on a metabolic phantom involving a 15 mm diameter outer tube of water, and three inner 5 mm tubes containing choline at ~10 mM (labeled I), creatine at ~50 mM (labeled II), and N-aceytl aspartate at ~50 mM (labeled III). **a**: Reference scout image. **b,c**: Reference spectra acquired in 32 scans using VAPOR water suppression (6) and LASER localization (top), and the spatially localized RE MRS sequence in Figure 1a incorporating a 30-ms multiband linear-phase equiripple pulse targeting the I–III resonances (bottom). The slightly lower intensity displayed by the NAA resonance can be traced to an inferior shimming at the position of tube III. **d**: Spectrally resolved images of the three components arising from a Relaxation-Enhanced but otherwise conventionally phase-encoded CSI sequence introduced in Figure 1b. **e**: Spectrally resolved images of the three targeted components arising from the multiscan shift-encoded SECSI sequence introduced in Figure 1c. **f**: Idem but for the single-scan multiecho SECSI MR sequence shown in Figure 1d. Regions of interests for SNR and for residual cross-talk level calculations were marked with squares in (a). The SNR for each image was measured by dividing the average of the corresponding component signals within the marked green/magenta/blue squares by the standard deviation of the noise in the red-marked square. The same markers were used to calculate residual cross-talk levels, by dividing the targeted signal by the residuals arising at the positions of the remaining two components. Common scan parameters: FOV = 20×20 mm^2, slice thickness = 4 mm, spatial matrix size = 64×64, $T_E = 144$ ms, $T_R = 5$ s. For the SECSI experiments, the shift-encoding parameters were $\tau = 1.248$ ms, $N = 8$. Number of signals averaged and total acquisition times were as follows. For (d): single shot per increment; total scan time 5 h 41 min. For (e): eight-shot average and total scan time 42 min 40 s. For (f) 256 shots averaged and total time 42 min 40 s (including reference scans).

expectation for this ratio is simplified by the fact that excitation and spatial acquisition parameters were kept constant among the two experiments; theory then predicts

$$\frac{SNR_{SECSI}^{multi-scan}}{SNR_{CSI}} = \frac{\sqrt{N}}{\sqrt{N_x}} \cdot \frac{\sqrt{t_{acq}^{\delta}}}{\sqrt{\tau_{ro}}} \cdot \frac{\int_{-\tau_{ro}/2}^{\tau_{ro}/2} e^{-|t|/T_2^*}\, dt}{\int_0^{t_{acq}^{\delta}} e^{-|t|/T_2^*}\, dt}. \quad [9]$$

With the number of points collected and acquisition times used known, only the exact value of T_2^* to be used in this evaluation is not precisely defined. A reasonable estimate of $T_2^* = 30$ ms predicts this ratio to be 0.98. The higher than expected SNR evidenced by the multiscan SECSI probably reflects instrumental and processing aspects that affect the SNR estimation. We find, for instance, that phasing the CSI data is complicated by residual eddy currents that do not affect the SECSI acquisitions due to their much larger spectral bandwidths and shorter acquisition times. Similar biases favoring SECSI's sensitivity over CSI's were found in independent experiments collected at different field and on different samples (for instance in the cases presented in Supporting Information, Figures S3 and S4).

A similar SNR calculation can relate the efficiencies of the single- and the multi-shot SECSI experiments. Following normalization by their different number of signal averages, the data in Figures 3e, 3f show that this ratio will be $4.37^*\sqrt{(8/256)} = 0.77$. The theoretical expectation for this ratio is

$$\frac{SNR_{SECSI}^{single-scan}}{SNR_{SECSI}^{multi-scan}} = \frac{\sum_{j=1}^{N_{pe}} \exp[-j(N\tau + \Delta)]/T_2}{N_{pe}} \quad [10]$$

Assuming a T_2 value of 500 ms and the experimentally used N, τ, and Δ values, this leads to a per-scan ratio of ~0.52, in good agreement with the experimental. This ability of the single-scan approach to match the performance of its N_{pe}-times longer counterpart reflects the efficient use that the CPMG pulse train in the single-shot SECSI sequence makes of the short acquisition time, and the sensitivity gains that are to be made by echoing what are usually inhomogeneously broadened, but not necessarily short-T_2, spectral resonances. When compared against the even longer acquisition needs of a regular CSI experiment, the higher efficiency of the single-shot SECSI, and the high T_2/T_2^* ratios that will maximize this efficiency, become clear.

Figure 4 shows extensions of these phantom tests to ex vivo rat brain acquisitions at 14.1 T. Under these conditions, good metabolic maps were afforded by the SECSI sequence for tCho, tCre and NAA after a couple of hours of signal averaging; by contrast, RE phase-encoded CSI images (not shown) remained poor even after ≥10 hr acquisition time. A similar instance of SECSI's SNR

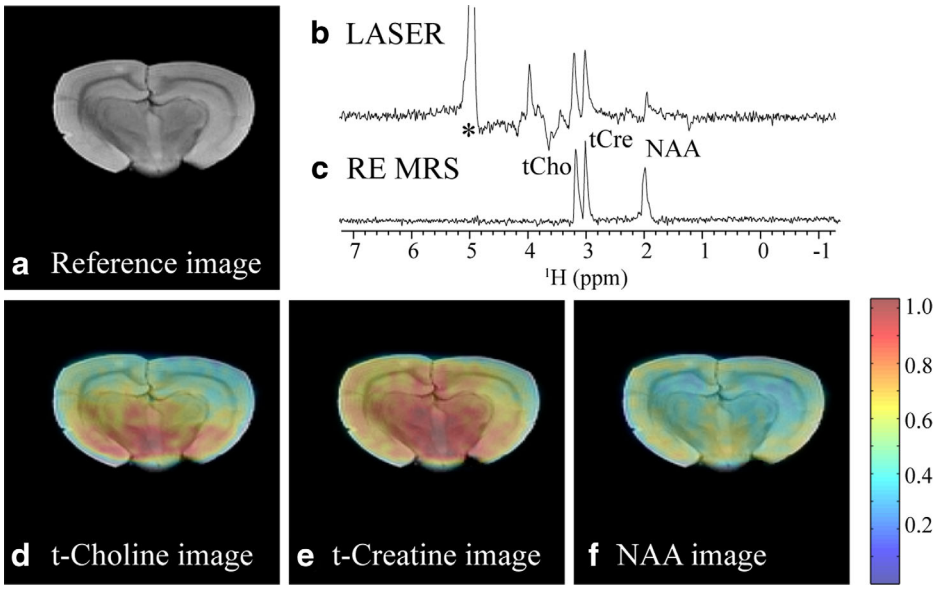

FIG. 4. Ex vivo rat brain results arising from experiments recorded at 14.1 T. **a**: Reference SEMS image. **b,c**: Reference LASER-localized and RE ^{1}H MRS spectra acquired on a $20 \times 20 \times 4\,mm^3$ voxel using 32 averages; (c) used the sequence in Figure 1a with a 30 ms two-band pulse exciting total cholines and creatines in one band, and NAA in another. The slightly lower intensity displayed by the NAA resonance can be traced to this metabolite's decay postmortem (36). **d–f**: tCho, tCr, and NAA maps (overlaid on anatomical images) arising from the execution of the SECSI sequence in Figure 1d, and reconstructed using the Matlab®-based algorithm described in the Supporting Information. Scan parameters: FOV = $20 \times 20\,mm^2$, slice thickness = 4 mm, matrix size = 32×32, echo time = 144 ms, TR = 5 s, $\tau = 1.276$ ms, $N = 8$, number of averages = 2048, experimental time = 5 h 41 min (including the reference scans). The colorbar represents relative intensities, normalized with respect to each image's maximum/minimum amplitudes.

improvement versus CSI is illustrated in the Supporting Information Figure S4, for mice data collected at 7T. In both cases, we ascribe this differences in SNR to SECSI's reliance on a CPMG train, capable of overcoming T_2^* losses.

Finally, Figure 5 demonstrates an application of these strategies to the spectroscopic imaging of fat and water peaks resonating at 4.8 and 1.5 ppm, respectively, in a live mouse. Because of the good sensitivity of this abdominal experiment, the possibility arose of exploiting the single-shot nature of the SECSI sequence in Figure 1d. Limiting this potential, however, were the relatively short T_2s of the targeted species. Analysis of this system indicated that at 7T a stable separation of the two sites would result from $N = 3$ echoes separated by $\tau = 0.668$ ms. If these parameters were inserted in the multiscan phase encoded sequence illustrated in Figure 1c, the result would be a three-point Dixon-like water/fat separation sequence (15). Figures 5b and 5d illustrate the retrieval of such images in a single (plus a reference) scan; the correspondence with images collected in multiple shots in the presence of fat or water suppression (Figs. 5a,c), is evident.

DISCUSSION AND CONCLUSIONS

The encoding modes used by the SECSI sequences here illustrated leverage several complementary aspects, deriving from an a priori knowledge of the resonance positions assumed by the RE MRS experiment. These include (i) the sparse nature of these resonances, which makes their discrimination by means of a short number of delays feasible; (ii) the possibility of concatenating these encoding delays in a train of gradient echoes, adding a spatial dimension to the spectral decoding procedure while retaining the experiment's single-scan nature; and (iii) the shortness of the ensuing gradient echo train, enabling its concatenation within a CPMG loop capable of phase-encoding an additional spatial axis. This leads to a significant compression of what eventually becomes a 2D spatial / 1D spectral single-shot acquisition. The single-shot nature of the experiment might find usefulness in hyperpolarized ^{13}C MRSI scenarios, where rapid acquisitions are of essence and spectral sparseness very common.

Although SECSI's single-shot nature might be of more limited use when targeting ^{1}H resonances at conventional metabolic concentrations, the method can still provide a higher sensitivity per unit time than conventional phase-encoded CSI counterparts; this results from the additional sensitivity endowed by a spin-echoed vis-à-vis a regular FID acquisition. Interestingly, when applied on a two-site system, the ensuing sequence becomes a multiple gradient- and spin-echoed version of the Dixon water–fat separation experiment, which is the archetypical in vivo scenario where the targeted frequencies are a priori known. Also worth remarking is the method's similarity with EPSI, a single-shot 2D spectral/spatial correlation technique based as well on oscillating gradients (31–33). For characterizing its spectroscopic dimension, however, EPSI does not make any assumption; hence, it will have to oscillate its gradient numerous times at a period given by an arbitrary spectral bandwidth one is trying to characterize. SECSI by contrast assumes that the peak offsets are known, and what is being sought is

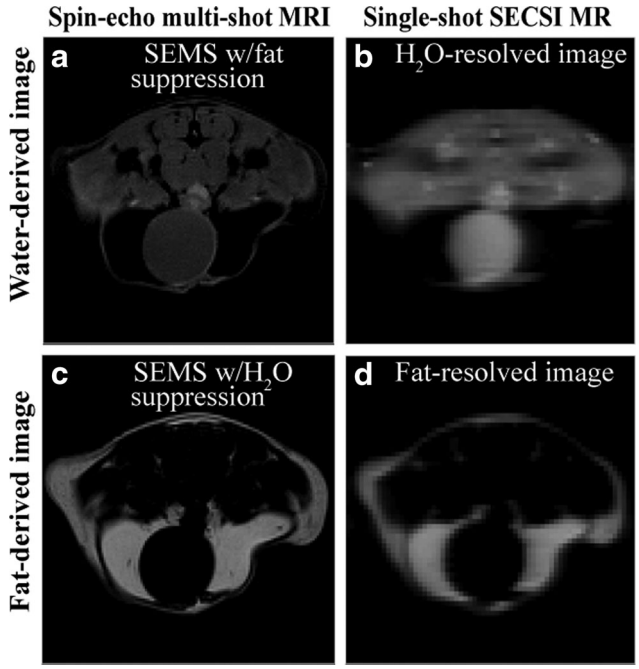

FIG. 5. In vivo fat/water separation capabilities of the SECSI sequence in Figure 1d, as applied to 7T abdominal mouse investigations. **a,c**: Multiscan spin echo references involving fat suppression (a) and water suppression (c). **b,d**: Water- (b) and fat-tissue (d) images separated by single-scan SECSI. Common imaging parameters: FOV = $32 \times 32\,mm^2$, TR = 2 s, TE = 14 ms, slice thickness = 2 mm. The reference image matrix size was 128×128; due to the short T_2s the SECSI image size was limited to 64×64, which explains the lower resolution. Total scan time for each spin-echo multiscan image: 4 min 16 s. Total SECSI acquisition time (including a reference navigator scan): 4 s.

just the minimal number of echoes capable of discriminating the targeted peaks.

Notwithstanding these benefits, several factors may challenge SECSI's effectiveness. Foremost among these are any issues that compromise the experiment's sparse spectral assumption. Indeed, if executed at low magnetic fields, if attempting to separate too many resonances, or if investigating systems that are spectrally crowded, the excitation pulses may become too long and/or decoding gradients require too high a number N of echoes. T_2-derived losses may in any of these cases become too onerous to make the approach competitive. This makes the approach less interesting for lower-field ($\leq$3T) applications; higher field human scanners, however, should benefit from similar advantages as demonstrated in Figure 4. Less important are field inhomogeneity and chemical shift dispersion effects, for which the condition number of the chemical shift encoding matrix can often be optimized without increasing the number of gradient echoes. Field fluctuations changing in unison all resonances positions should also be well tolerated by this algorithm, which only depends on chemical shift differences. A final aspect that conspires against an optimal SECSI operation, arises from the need to collect reference scans to enable a suitable co-processing of the phase-encoded k-space. While reference scans are easily incorporated into sensitive EPI acquisitions, they can significantly increase experimental times in low sensitivity MRSI investigations. It is hoped that either improvements in the imaging hardware and/or referenceless methods developed to deal with phase corrections in EPI-based experiments (34,35), may also be useful in the present approach. This would be of particular value not only in low-sensitivity ^{1}H MRSI experiments like those illustrated in this study, but also in other experiments on sparse resonances like ^{31}P MRSI investigations.

ACKNOWLEDGMENTS

We are grateful to Amir Seginer for assistance in the development of the low-conditioned number algorithm, to Dr. Nava Nevo (WIS Veterinary Services) for the mouse brain specimens, and to Koby Zibzener for assistance in the acquisition of the experiments. This work was funded by the Israel Science Foundation, the Kimmel Magnetic Resonance Institute (Weizmann), and by the generosity of the Perlman Family Foundation. NS was supported in part by the European Union's Horizon 2020 research and innovation programme under the Marie Sklodowska-Curie grant agreement No 657366 Z.Z. is thankful for financial support from the China Scholarship Council.

REFERENCES

1. Barker PB, Lin DDM. In vivo proton MR spectroscopy of the human brain. Prog Nucl Magn Reson Spectrosc 2006;49:99–128.
2. Bradley WG, Brant-Zawadzki M, Cambray-Forker J. MRI of the brain. Philadelphia: Lippincott Williams & Wilkins; 2001.
3. De Graaf RA. In vivo NMR spectroscopy: principles and techniques. New York: John Wiley & Sons; 2008.
4. Haase A, Frahm J, Hanicke W, Matthaei D. ^{1}H NMR chemical shift selective (CHESS) imaging. Phys Med Biol 1985;30:341.
5. Piotto M, Saudek V, Sklenar V. Gradient-tailored excitation for single-quantum NMR spectroscopy of aqueous solutions. J Biomol NMR 1992;2:661–665.
6. Tkac I, Starcuk Z, Choi IY, Gruetter R. In vivo 1H NMR spectroscopy of rat brain at 1 ms echo time. Magn Reson Med 1999;41:649–656.
7. Ogg RJ, Kingsley PB, Taylor JS. WET, a T_1- and B_1-insensitive water-suppression method for in vivo localized ^{1}H NMR spectroscopy. J Magn Reson B 1994;104:1–10.
8. van Der Veen JW, Weinberger DR, Tedeschi G, Frank JA, Duyn JH. Proton MR spectroscopic imaging without water suppression. Radiology 2000;217:296–300.
9. Clayton DB, Elliott MA, Lenkinski RE. In vivo proton spectroscopy without solvent suppression. Conc Magn Reson 2001;13:260–275.
10. Dong Z, Dreher W, Leibfritz D. Toward quantitative short-echo-time in vivo proton MR spectroscopy without water suppression. Magn Reson Med 2006;55:1441–1446.
11. Shemesh N, Dumez J-N, Frydman L. Longitudinal relaxation enhancement in ^{1}H NMR spectroscopy of tissue metabolites via spectrally selective excitation. Chemistry 2013;19:13002–13008.
12. de Graaf RA, Behar KL. Detection of cerebral NAD(+) by in vivo ^{1}H NMR spectroscopy. NMR Biomed 2014;27:802–809.
13. Shemesh N, Rosenberg JT, Dumez JN, Grant SC, Frydman L. Metabolic T_1 dynamics and longitudinal relaxation enhancement in vivo at ultrahigh magnetic fields on ischemia. J Cereb Blood Flow Metab 2014;34:1810–1817.
14. Shemesh N, Rosenberg JT, Dumez J-N, Muniz JA, Grant SC, Frydman L. Metabolic properties in stroked rats revealed by relaxation-enhanced magnetic resonance spectroscopy at ultrahigh fields. Nat Commun 2014;5:4:958.
15. Glover GH, Schneider E. Three-point Dixon technique for true water/fat decomposition with B_0 inhomogeneity correction. Magn Reson Med 1991;18:371–383.
16. Xiang QS, An L. Water-fat imaging with direct phase encoding. J Magn Reson Imaging 1997;7:1002–1015.

17. Reeder SB, Brittain JH, Grist TM, Yen YF. Least-squares chemical shift separation for ^{13}C metabolic imaging. J Magn Reson Imaging 2007;26:1145–1152.
18. Silver MS, Joseph RI, Hoult DI. Selective spin inversion in nuclear magnetic resonance and coherent optics through an exact solution of the Bloch-Riccati equation. Phys Rev A 1985;31:2753–2755.
19. Conolly S, Glover G, Nishimura D, Macovski A. A reduced power selective adiabatic spin-echo pulse sequence. Magn Reson Med 1991; 18:28–38.
20. Garwood M, DelaBarre L. The return of the frequency sweep: designing adiabatic pulses for contemporary NMR. J Magn Reson 2001;153: 155–177.
21. Brown TR, Kincaid BM, Ugurbil K. NMR chemical shift imaging in three dimensions. Proc Natl Acad Sci U S A 1982;79:3523–3526.
22. Maudsley AA, Hilal SK, Perman WH, Simon HE. Spatially resolved high resolution spectroscopy by "four-dimensional" NMR. J Magn Reson 1983;51:147–152.
23. Zhang ZY, Smith PES, Frydman L. Reducing acquisition times in multidimensional NMR with a time-optimized Fourier encoding algorithm. J Chem Phys 2014;141:194201.
24. Chandrashekar S, Shrot Y, Frydman L. A double-Fourier approach to enhance the efficiency of the indirect domain sampling in 2D NMR. Magn Reson Chem 2011;49:477–482.
25. Feinberg DA, Oshio K. GRASE (gradient- and spin-echo) MR imaging: a new fast clinical imaging technique. Radiology 1991;181:597–602.
26. Oshio K, Feinberg DA. GRASE (Gradient- and spin-echo) imaging: a novel fast MRI technique. Magn Reson Med 1991;20:344–349.
27. Carr HY, Purcell EM. Effects of diffusion on free precession in nuclear magnetic resonance experiments. Phys Rev 1954;94:630–638.
28. Meiboom S, Gill D. Modified spin-echo method for measuring nuclear relaxation times. Rev Sci Instrum 1958;29:688–691.
29. Pohmann R, von Kienlin M, Haase A. Theoretical evaluation and comparison of fast chemical shift imaging methods. J Magn Reson 1997;129:145–160.
30. Pauly J, Le Roux P, Nishimura D, Macovski A. Parameter relations for the Shinnar-Le Roux selective excitation pulse design algorithm. IEEE Trans Med Imaging 1991;10:53–65.
31. Webb P, Spielman D, Macovski A. A fast spectroscopic imaging method using a blipped phase encode gradient. Magn Reson Med 1989;12:306–315.
32. Posse S, Dager SR, Richards TL, Yuan C, Ogg R, Artru AA, Müller-Gärtner H-W, Hayes C. In vivo measurement of regional brain metabolic response to hyperventilation using magnetic resonance: proton echo planar spectroscopic imaging (PEPSI). Magn Reson Med 1997; 37:858–865.
33. Mansfield P. Spatial mapping of the chemical shift in NMR. Magn Reson Med 1984;1:370–386.
34. Buonocore MH, Gao LS. Ghost artifact reduction for echo planar imaging using image phase correction. Magn Reson Med 1997;38:89–100.
35. Bruder H, Fischer H, Reinfelder HE, Schmitt F. Image reconstruction for echo planar imaging with nonequidistant k-space sampling. Magn Reson Med 1992;23:311–323.
36. Petroff OA, Ogino T, Alger JR. High-resolution proton magnetic resonance spectroscopy of rabbit brain: regional metabolite levels and postmortem changes. J Neurochem 1988;51:163–171.
37. Bottomley PA. Spatial localization in NMR spectroscopy in vivo. Ann N Y Acad Sci 1987;508:333–348.

SUPPORTING INFORMATION

Additional Supporting Information may be found in the online version of this article.

Fig. S1. Traversing of the (k_{ro},k_{pe},τ_n) space in the single-shot SECSI acquisition protocol, highlighting details of the chemical shift encoding and decoding modes. **a**: Expanded acquisition block of the sequence, showing only the first and last acquisition gradient echoes for each phase encoding step. **b**: Trajectories imposed on the spins' evolution along the chemical shift encoding, the k_{ro} and the k_{pe} imaging dimensions, highlighting the positions of 10 instants marked in the sequence (a). Green arrows represent k_{ro}-axis traces scanned during six hypothetical readout gradients for each chemical-shift-encoding train; the dotted green lines next to them represent the trajectories imposed by the corresponding refocusing gradients. The solid cyan lines show the jumps along k_{pe} imposed by the phase encoding gradient blips, while the dark blue ones are those imposed by the refocusing pulses; notice in this case the alternating changes in k_{pe} values. In each phase encoding step the signals collected in the presence of positive readout gradients ($k_{pe} \leq 0$; darker green colors) are modulated by $\{E_{mn}\}$, while those recorded during negative readout gradients ($k_{pe} > 0$; lighter green) are modulated by $\{E^*_{mn}\}$. **c**: Details of the chemical shift decoding procedure. The $N \times N_{pe}$ full k_{ro}-space echoes carrying the chemical shift encoded information, are separated into two matrices according to the sign of the readout gradient used. For each phase-encoded value, the N echoes recorded in the presence of positive readout gradients are decoded by the inverse of the encoding matrix $\{E_{mn}\}$, while shift-encoded signals recorded while in the presence of negative readout gradients are decoded by the inverse of $\{E^*_{mn}\}$. Each of the ensuing 2D k-space data sets is then fast FT for retrieving what in principle are identical spectrally resolved images (procedure not shown); these can be co-added for the sake of improving sensitivity.

Fig. S2. Comparison of ex vivo mouse brain RE MRS ^1H traces obtained before and after the acquisition of SECSI RE CSI experiments, recorded at 7T. The sample was prepared and preserved as described in the Methods section.

Fig. S3. Comparing the spectroscopic imaging results from a phantom sample involving water, methanol (I), acetone (II) and cyclohexane (III), examined at 7T using various RE and SECSI sequences. **a**: Reference spin-echo multishot image. **b**: Reference spectrum acquired by PRESS, delivering the spectral information required to design the SLR pulse (the small unlabeled resonance at ~5.5 ppm corresponding to the untargeted –OH methanol site; the chemical shifts of the targeted resonances deviate by ca. 0.7 ppm from the literature values reported for these chemicals, owing to susceptibility-induced differences arising in this multicompartment phantom.) **c,d**: Spectra acquired using the spatially localized RE MRS sequence in Figure 1a, in well shimmed and in poorly shimmed magnetic fields, respectively. A 40 ms multiband linear-phase equiripple pulse was used to excite the (I, II, and III) resonances; the line widths of resonance III were 12 Hz in (c) and 75 Hz in (d). **e**: Spectrally resolved images of the three components arising from a Relaxation-Enhanced but otherwise conventionally phase-encoded CSI sequence like the one introduced in Figure 1b, collected in the well-shimmed field. **f,g**: Spectrally resolved images of the three targeted components arising from the multiscan shift-encoded SECSI sequence introduced in Figure 1c, collected in a well-shimmed and in an inhomogeneous field, respectively. **h,i**: Idem but for the single-scan multiecho SECSI MR sequence shown in Figure 1d. Regions of interests for SNR and for residual cross-talk level calculations were marked with squares in (a). The SNR for each image was measured by dividing the average of the corresponding component signals within the marked green/magenta/blue squares by the standard deviation of the noise in the red-marked square. The same markers were also used to calculate residual levels in panels (e–i), by dividing the targeted signal by the residuals arising at the positions of the remaining two components. Common scan parameters: FOV = 40×40 mm^2, slice thickness = 2 mm, two dummy scans, echo time- = 50 ms, TR = 5 s, averages nt = 1. For the SECSI experiments, the shift-encoding parameters were $\tau = 1.002$ ms, $N = 6$. The matrix size for (e) was 64×64 and its total scan time is 5 h 41 min. Matrix sizes for (f), (g), (h), and (i) were 128×128; total scan times for (f) and (g) were 10 min 40 s, while scan times for (h) and (i) were only 20 s.

Fig. S4. Comparison of ex vivo mouse brain results arising from SECSI and from a RE CSI sequences recorded at 7T. **a**: Reference SEMS image. **b,c**: Reference PRESS and RE MRS spectra acquired on a $16 \times 16 \times 4$ mm^3 voxel using 32 averages; (c) used the sequence in Figure 1a with a 40 ms two-band pulse exciting the total cholines and creatines in one band, and NAA in another. **d–f**: Cho, Cr, NAA maps (overlaid on anatomical T_1-weighted images) arising from the execution of the SECSI sequence in Figure 1d, and reconstructed using the Matlab®-based algorithm described in the Supporting Information. **g–i**: Idem but for acquisitions based on a RE CSI sequence. Common scan parameters: FOV = 16×16 mm^2, slice thickness = 4 mm, matrix size = 32×32, echo time = 50 ms, TR = 2 s. SECSI parameters: $\tau = 1.524$ ms, $N = 8$, number of averages = 2048. The number of averages for the RE CSI sequence was eight per phase-encoding value. The experimental time of the SECSI MRSI experiment was 2 h 16 min (including the reference scans), while the phase-encoded CSI acquisition took 4 h 33 min). The colorbar represents relative intensities.